A TRIDENT SCHOLAR PROJECT REPORT

NO. 498

Characterization of the Far-Wake of a 6:1 Prolate Spheroid

by

Midshipman 1/C Jonathan P. Peck, USN

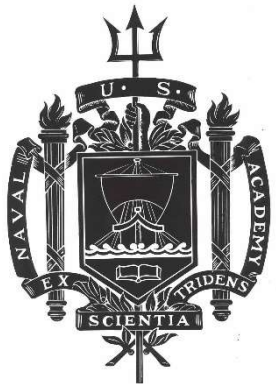

UNITED STATES NAVAL ACADEMY
ANNAPOLIS, MARYLAND

USNA-1531-2

REPORT DOCUMENTATION PAGE

Form Approved
OMB No. 0704-0188

1. REPORT DATE *(DD-MM-YYYY)*	**2. REPORT TYPE**	**3. DATES COVERED** *(From - To)*
7/6/20		

4. TITLE AND SUBTITLE
Characterization of the Far-Wake of a 6:1 Prolate Spheroid

5a. CONTRACT NUMBER

5b. GRANT NUMBER

5c. PROGRAM ELEMENT NUMBER

6. AUTHOR(S)
Peck, Jonathan P.

5d. PROJECT NUMBER

5e. TASK NUMBER

5f. WORK UNIT NUMBER

7. PERFORMING ORGANIZATION NAME(S) AND ADDRESS(ES)

8. PERFORMING ORGANIZATION REPORT NUMBER

9. SPONSORING / MONITORING AGENCY NAME(S) AND ADDRESS(ES)
U.S. Naval Academy
Annapolis, MD 21402

10. SPONSOR/MONITOR'S ACRONYM(S)

11. SPONSOR/MONITOR'S REPORT NUMBER(S)
Trident Scholar Report no. 498 (2020)

12. DISTRIBUTION / AVAILABILITY STATEMENT

This document has been approved for public release; its distribution is UNLIMITED.

13. SUPPLEMENTARY NOTES

14. ABSTRACT

Even with the dramatic advances in computational power seen in the last decades, Computational Fluid Dynamics (CFD) models are as yet unable to predict transition, separation, and wake development for fluid flow over three-dimensional bodies to the desired level of accuracy in an acceptable amount of time. Without the ability to predict forces and moments experienced by the body, critical parameters such as drag and loads on control surfaces for air- and water-borne vehicles cannot be predicted. The prolate spheroid has long been a popular body upon which to verify CFD models because of its simple geometry and three-dimensional flow field. Advances in computational speed and experimental capabilities have prompted a renewed interest in related research.

An experiment was conducted in the large towing tank facility of the U.S. Naval Academy, using a 6:1 prolate spheroid, measuring 54 in. (1.4 m) in length and 9 in. (0.23 m) in diameter. The spheroid model was inclined by 15° relative to the undisturbed free surface, and towed at speeds yielding length-based Reynolds numbers from $0.5\text{-}4.2\times10^6$. The results from the 0.5×10^6 case are presented in the present discussion. A stationary stereo particle image velocimetry (SPIV) system was designed for the experiment and used to provide two-dimensional velocity maps in two spatial-dimensions (2C2D). These time histories show the trajectory of the wake as it leaves the tail of the model, the expansion of the wake width, the size, strength, and position of the primary vortical structures shed into the wake. These results will inform follow-on studies focused on measuring turbulent quantities in the far wake.

15. SUBJECT TERMS
Prolate spheroid, wake survey, towing tank

16. SECURITY CLASSIFICATION OF:			**17. LIMITATION OF ABSTRACT**	**18. NUMBER OF PAGES**	**19a. NAME OF RESPONSIBLE PERSON**
a. REPORT	**b. ABSTRACT**	**c. THIS PAGE**		31	**19b. TELEPHONE NUMBER** *(include area code)*

U.S.N.A. --- Trident Scholar project report; no. 498 (2020)

CHARACTERIZATION OF THE FAR-WAKE OF A 6:1 PROLATE SPHEROID

by

Midshipman 1/C Jonathan P. Peck
United States Naval Academy
Annapolis, Maryland

_____

(signature)

Certification of Adviser(s) Approval

LCDR Ethan Lust
Mechanical Engineering Department

_____

(signature)

_____

(date)

Acceptance for the Trident Scholar Committee

Professor Maria J. Schroeder
Associate Director of Midshipman Research

_____

(signature)

_____

(date)

Abstract

Even with the dramatic advances in computational power seen in the last decades, Computational Fluid Dynamics (CFD) models are as yet unable to predict transition, separation, and wake development for fluid flow over three-dimensional bodies to the desired level of accuracy in an acceptable amount of time. Without the ability to predict forces and moments experienced by the body, critical parameters such as drag and loads on control surfaces for air- and water-borne vehicles cannot be predicted. The prolate spheroid has long been a popular body upon which to verify CFD models because of its simple geometry and three-dimensional flow field. Advances in computational speed and experimental capabilities have prompted a renewed interest in related research.

An experiment was conducted in the large towing tank facility of the U.S. Naval Academy, using a 6:1 prolate spheroid, measuring 54 in. (1.4 m) in length and 9 in. (0.23 m) in diameter. The spheroid model was inclined by 15° relative to the undisturbed free surface, and towed at speeds yielding length-based Reynolds numbers from 0.5-4.2×10^6. The results from the 0.5×10^6 case are presented in the present discussion. A stationary stereo particle image velocimetry (SPIV) system was designed for the experiment and used to provide two-dimensional velocity maps in two spatial-dimensions (2C2D). These time histories show the trajectory of the wake as it leaves the tail of the model, the expansion of the wake width, the size, strength, and position of the primary vortical structures shed into the wake. These results will inform follow-on studies focused on measuring turbulent quantities in the far wake.

This research is funded by the Office of Naval Research, Advanced Naval Platforms Division (ONR 331), contract number N0001419WX01094.

Keywords
Prolate spheroid, wake survey, towing tank

Acknowledgements

In addition to acknowledging the generous support of our sponsor, Dr. Peter Chang at the Office of Naval Research, I would like to acknowledge the support of our collaborator, Dr. Matthew Jemison at NSWC Carderock for his assistance in providing preliminary CFD simulations. I would also like to thank the dedicated staff of the Hydromechanics Laboratory, including Mr. Alex Laun, Mr. Bill Beaver, Mr. Michael Stanbro, Mr. John Balano, and Mr. Adam King for their many collective hours of assistance and support. I would also like to thank the staff of the Project Support Branch for assisting with the design of, and the manufacturing of the major components of the experimental apparatus; particularly Mr. Tom Price, Mr. Nicholas Hlavaty, Mr. Brandon Stanley, and Mr. Michael Koivula. I would like to thank Prof. Josh Radice for his assistance in the vibration analysis of the experimental apparatus. Finally, I would like to thank Ms. Victoriia Grabovetska, our ONR SEAP summer intern for her contributions to the experimental design.

TABLE OF CONTENTS

Abstract 1
Acknowledgements 1
Background 3
Theory 4
  Reynolds Number 4
  Particle Image Velocimetry 6
Literature Review 7
Materials and Methods 9
Results and Discussion 13
  Wake Characterization 13
  Vortex Characterization 17
Conclusions and Summary 23
Future Work 24
Bibliography 25
Appendix A 28

Background

The Office of Naval Research Advanced Naval Platforms Division (ONR 331) is responsible for advancing research in a variety of subject areas. Much of the work supported by code 331 is focused on the first stage of the technological development process: basic research. In this regard, their goal is to support research activities with the broadest possible application and impact, laying the foundation for the cutting-edge applied research to follow. One of the selected pathways to this goal is to leverage new and significantly more powerful computational and experimental techniques to further understanding and prediction of next-generation vehicles; everything from aircraft and unmanned aerial vehicles (UAVs) to surface ships and unmanned underwater vehicles (UUVs).

Ideally, air- and water-borne vehicles would be designed primarily with computers, including computational fluid dynamics (CFD) tools to predict the velocity and pressure distribution around the body and into the wake. From these, the desired design parameters would be determined including the forces and moments imposed on the body by the fluid, the length and time scales of the wake structures, and the acoustic characteristics of the design, as examples. The number of experiments required from ideation to production – often expensive and time-consuming to conduct – would be minimized in this ideal case. Despite significant advancements in computational power and numerical prediction capabilities in recent decades, three-dimensional flows cannot currently be modeled with the desired level of accuracy in an acceptable amount of time. Experiments at a range of scales are required to validate CFD results for a particular design in order to provide the confidence necessary to progress from design to production.

The computational power required to model fluid flow at the range of length and time scales necessary to produce accurate predictions is not yet available and is unlikely to be achieved with computers as we know them today, however powerful they become in the future. A number of simplifications and approximations are therefore made in order to arrive at a useful solution in an acceptable amount of time. These approximations are often based on experimental observations of the fundamental physics that govern fluid behavior. A dedicated experimental campaign and a closer examination of the empirical results may provide the insight necessary to improve computational tools such that fewer experiments are ultimately needed.

This study, the first of a series of related experiments, is focused on the wake of a canonical body of revolution, the 6:1 prolate spheroid – an axisymmetric body in the shape of a revolved ellipse. The ratio 6:1 is the ratio of the length to the major diameter of the spheroid. Flow around prolate spheroids, particularly when the flow direction is not parallel to the major axis of the body, is hydrodynamically rich. As will be described in the next section, the boundary layer development along the body is complex. Depending on the flow conditions, there are multiple separation points, creating multiple sets of vortex sheets that are released into the wake. The turbulence generated near the body is bound up by these vortex structures and changes the character of the coherent structures shed by the body. Not only is there considerable interest in learning more about these flow features, but there is also a great deal of interest in using the resulting data to develop computational fluid dynamics (CFD) codes that can more accurately represent them. It is the aim of this study to characterize the trajectory and length scales of the wake as it evolves downstream

of the body and to examine the large coherent structures in the wake and estimate the time scales of these dominant features.

Theory

Reynolds Number

The wake produced by flow around a submerged or partially-submerged body is familiar to anyone who has stood observant on the bank of a fast running river. Near the banks, the flow moves slow and the region just downstream of the rocks is quiet and smooth; moving nearly imperceptibly. Out near the middle where the water is moving fast, the region just downstream of a boulder is foamy, chaotic, and raging. In fluid dynamics, a parameter called the Reynolds number is used to describe these two flows quantitatively.

The Reynolds number is a ratio of the inertial forces to the viscous forces in a flow. Its exact definition depends on the specific flow scenario, but for the purposes of this discussion, it is defined as:

$$Re_\ell = \frac{U\ell}{\nu} \tag{1}$$

Where U is the velocity of the surrounding fluid, ℓ is the characteristic length of the solid body in the flow, and ν is the kinematic viscosity of the fluid. Thinking back to the river, the first scenario of the slow, burbling flow around a rock likely has a Reynolds number on the order of 10 or 100. There is very little discernable wake downstream of the rock. Everything is calm and serene. In the second scenario, the Reynolds number is on the order of 100,000 or 1,000,000 or higher. The wake is energetic and highly turbulent. The power of the Reynolds number is that for any similarly-shaped body of any scale awash in any fluid – liquid or gas – if the Reynolds number is the same, the flow around the body and just downstream in the wake will look similar and have similar characteristics. This fact allows the comparison of flows at different scales; the representation of a full-sized ocean-going vessel (commonly referred to as the *prototype*) by a much smaller scale *model*, for example.

Generally, as Reynolds number increases, the flow around and immediately downstream of a body becomes more and more turbulent. However, at and above some upper value of the Reynolds number the flow and wake characteristics cease changing in any appreciable way. This is referred to as Reynolds number independence. In many experiments, the scales of the model and prototype are such that the Reynolds number cannot be matched. In this case, since the *prototype* Reynolds number is often sufficiently large to achieve independence, standard practice is to achieve as high a *model* Reynolds number as possible, ideally also above the number required for independence.

As a practical matter of experimentation, the Reynolds number is increased by increasing the velocity because the size of the model, the density of the fluid, and the viscosity of the fluid are typically much more difficult to change. Reynolds number independence is typically demonstrated by showing that the characteristics of the wake (e.g. the wake velocity profile or other calculated

quantities such as turbulence statistics) converge with increasing Reynolds number and remain approximately equal after it has said to have been achieved.

As discussed above, the Reynolds number is used to describe the transition from smooth, laminar flow to chaotic, turbulent flow. At the tip of the spheroid, the Reynolds number is small and the flow is smooth. As the flow moves down the body, the Reynolds number (again a function of length, in this case the downstream distance from the tip) increases and at some downstream distance transitions to turbulence. The downstream distance at which this transition occurs is a function of a number of parameters such as the flow speed, the surface roughness of the body, and the curvature of the body, as examples. Because the spheroid is inclined to the direction of the incoming flow, this transition occurs at different downstream distances around the circumference of the body, giving an asymmetry to the resulting near-body flow.

The relative speed of the flow near the body is zero, which is to say that the fluid "sticks" to the body regardless of how fast the surrounding flow is moving. The velocity increases from zero at the body to the free stream speed and direction some short distance away. When the flow velocity changes with position, this is called *velocity shear*. The distance from the body at which the velocity recovers to that of the free stream is called the *boundary layer*. Again, because the spheroid is inclined relative to the direction of the oncoming flow, the boundary layer (i.e. how thick it is and the location in the flow where it transitions from laminar flow to turbulent flow) is different at each point on the body and said to be three-dimensional. Predicting this behavior accurately is a goal of those who develop CFD tools and those tools cannot be validated without experimental data.

At higher Reynolds numbers, the inertia of a fluid is such that it cannot follow the curved path around the rear of the body. Due to the viscosity of the fluid, the fluid particles moving around a curved body lose kinetic energy. Since there is an increase in pressure along the direction of the flow on the rear half of the spheroid, this loss in energy results in the fluid not being able to travel against the adverse pressure gradient. Thus, the fluid particles will eventually separate in a process called *boundary layer separation*. Once the flow is separated from the body, the flow on the upper part of the boundary layer is moving at a higher velocity than the flow further inwards due to the viscous interaction of the fluid with the spheroid. This results in the flow developing a circular motion, ultimately shedding a pair of vortex sheets. Since momentum must be conserved, the two vortex sheets rotate in opposing directions. This is shown in Figure 1.

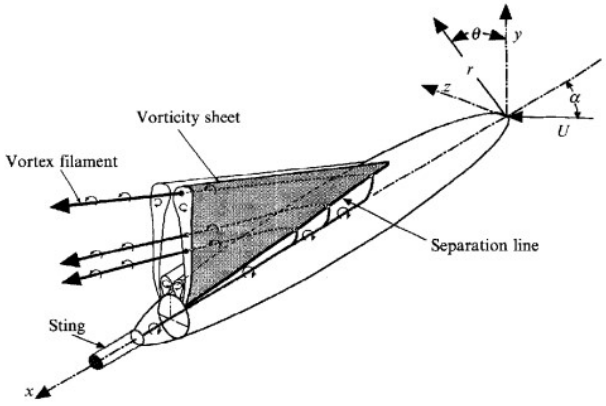

Figure 1: A visual representation of the expected vortex sheets to be shed from the body of the spheroid *[1]*.

As discussed previously, the two vortex sheets will be shed from the body of the spheroid at a distance that is dependent upon parameters such as flow speed, surface roughness, and the curvature of the body. As the Reynolds number increases, the boundary layer will separate further forward on the body of the spheroid, causing the vortices to form earlier and result in a more turbulent wake. At a sufficiently high Reynolds number, the characteristics of the wake will stop changing in an appreciable way as the Reynolds number approaches independence. Providing experimental results that quantify the wake in the independent regime is valuable in validating CFD predictions for large scale models.

Particle Image Velocimetry

Particle Image Velocimetry (PIV) is a technique used to measure the instantaneous velocity at a grid of points a flow field. The components of a PIV system are shown in Figure 2.

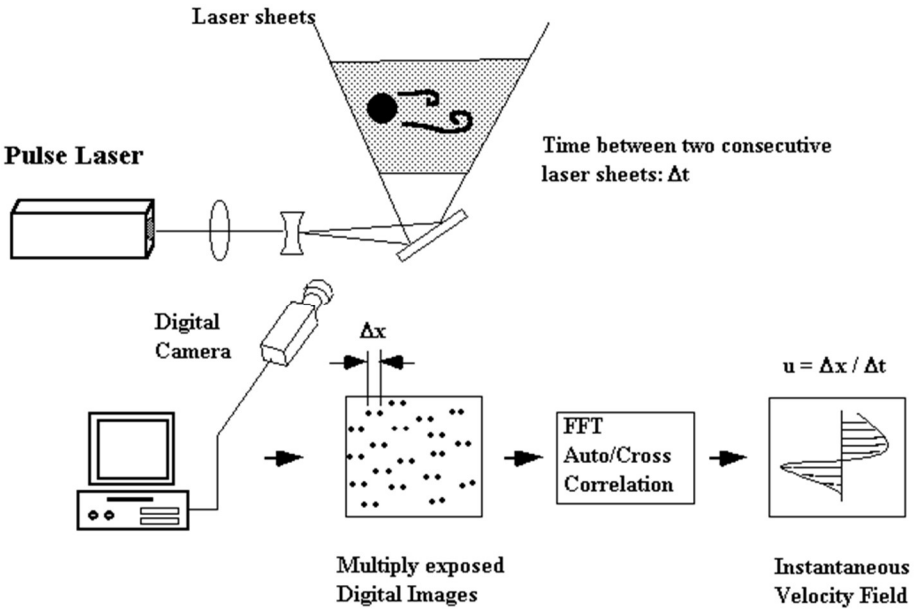

Figure 2: Diagram outlining the schematic of a PIV system *[2]*.

The flow of interest is seeded with neutrally buoyant particles that faithfully follow the flow. A digital camera is used to record two images of the instantaneous particle positions in quick succession. The two images are separated in time by a known time step, Δt that is variable depending upon the capture frequency of the camera and pulse frequency of the laser being used. A pulse laser is used to create a light sheet that illuminates the particles as the images are recorded like a high-intensity flash is used to take photographs of active subjects in low light. The images are processed using a data acquisition (DAQ) computer, and the particle displacements, Δx are calculated. From these displacements and the given time step between images, the instantaneous velocity can be determined. An additional camera can be used (not shown in the Figure) to measure the out-of-plane velocity, providing all three Cartesian velocity components for the measurement plane.

This entire system is controlled by software on the DAQ. In the case of this study, the system is controlled by Insight4G™. Image processing is completed by breaking images up into smaller spots for processing called interrogation regions. These interrogation regions are overlapped to allow for an additive process between regions that determines the peak correlation between the particles in two consecutive images. An example of this process is shown in Figure 3.

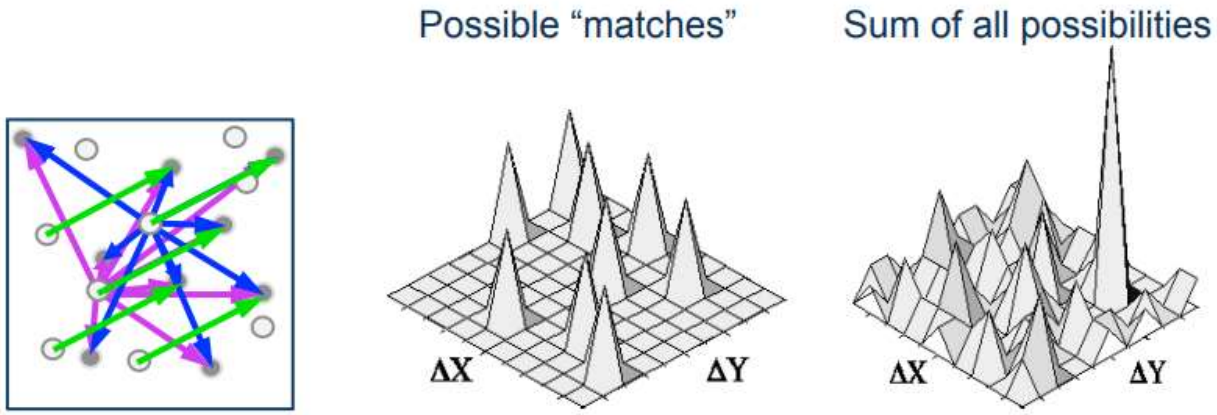

Figure 3: PIV particle correlation process. Interrogation region with potential particle displacements where hollow particles indicate initial position and filled particles indicate final position (left). Correlation peaks indicating the correlation between particles in the interrogation region (middle). Sum of all possible particle correlations in the interrogation region, resulting in a peak correlation (right) *[3]*.

The potential displacement of the particles is determined by looking at nearest neighbors for the particles in the interrogation region, shown on the left of Figure 3. The level of correlation between the particles in the interrogation region are shown on the correlation map in the middle of Figure 3. Using the overlap between interrogation regions, an additive process of all of the interrogation regions in the image determines the correlation peak. This peak correlation indicates the strongest relationship between two particles in the interrogation region. Thus, the selected particle pair is used to determine the actual particle movement in between the image frames.

Literature Review

A number of experimental studies on 6:1 prolate spheroids have focused on on-body and near wake flow characteristics. Meier and Kreplin obtained data on the boundary layer and separation region from flow visualization, surface hot film, and pressure measurements [4]. Reynolds numbers from 7.2 to 9.6×10^6 were tested at angles of attack from 0° to 30°. It was determined that an increase in Reynolds number moves the location of separation forward on the body and increases the magnitude of the shear stress. Angles of attack at or above 10° produce wholly different flow fields, shown by the change in location of separation lines. Barber and Simpson obtained boundary layer profiles and Reynolds shear stress measurements at two axial locations on the body of a 6:1 prolate spheroid for Reynolds numbers up to 4×10^6 and angles of inclination of 10° and 15° [5]. It was determined that near-body turbulence increased with Reynolds number and angle of inclination and that the boundary layer grows circumferentially and axially. Ahn and Simpson investigated the dependence of boundary layer transition and separation phenomena on angle of attack and Reynolds number [6]. A critical Reynolds number of approximately 2.5×10^6 was identified as being the transition point along the body from laminar to transitional and

turbulent separation. Results indicate that Reynolds number dependency of separation lines at Reynolds numbers above this critical value is greatly reduced. Fu et al. documented the effects of boundary layer tripping, angle of attack, and Reynolds number on the flow structure in the lee side of a prolate spheroid [1]. It was also one of the first studies to use Particle Image Velocimetry (PIV) to observe the near-body flow field around a prolate spheroid. Results showed that the pair of vortex sheets produced on either lateral side of the body increased in vorticity with Reynolds number and inclination. Results also indicated that the majority of the circulation in the flow lies outside of the distinct vortical structure of the flow. Goody, Simpson, and Engel employed the same model spheroid at the same angles of incidence at a Reynolds number of 4.2×10^6, measuring the velocity field with hot-wire velocimetry to further explore the near-body flow field [7]. At an inclination angle of 10° they showed that the turbulence was primarily located near the body, in contrast to observations at 20° in which the turbulence moved away from the body and into the wake region. Chesnakas and Simpson used a three-dimensional LDV system to record velocity measurements with corresponding wall-pressure measurements from $y^+ = 7$ out beyond the boundary layer edge [8]. The generation of secondary streamlines were determined to be the clearest indicator of separation, reattachment, and vortical structures in the flow. Most relevant to the current study is the existence of a region just behind the separation lines and between the two separation sheets that is relatively quiescent. Most of previous efforts were focused on near- or on-body flow behavior.

There are currently no experimental data documenting the flow phenomena in the far wake of a prolate spheroid. The far wake of a body of revolution is defined as the region past one body length downstream of the body ($x/L \geq 2.0$, referenced to the upstream tip of the body). In this region, the interaction of the leeward vortices is not understood, nor is the size, location, magnitude of vorticity, or dissipation rate. Therefore, a detailed experimental investigation of the far wake is the focus of this experimental study. As determined by Fu et al. [1] instantaneous velocity and vorticity distributions allow for the identification of primary and secondary vortices in the wake when the flow is both steady and unsteady. It is the objective of this study to determine the instantaneous velocity and vorticity distributions, observe wake evolution and meandering, the radius of the primary vortices, and determine the strength and time scale of their persistence. Flow was observed at Reynolds numbers from 0.5 to 4.2×10^6 at angles of attack of 15° and 20°. Only the data from the 15° case at 0.5×10^6 is presented here. In order to obtain instantaneous flow measurements in two dimensions, planar PIV is used.

Materials and Methods

Experiments were conducted in the United States Naval Academy large towing tank facility, which measures 116 m long, 7.9 m wide, and 4.9 m deep. The high-speed towing carriage used can achieve a maximum speed of 10 m/s.

The 6:1 prolate spheroid used in the present experiment measures 1.37 m (54 in.) long and is the same used in some of the canonical literature [1]. The model does not feature a boundary layer trip. The surface of the model was smoothed and refinished. All holes on the model were filled and smoothed. For the purposes of this discussion, the coordinate system used is shown in Figure 4.

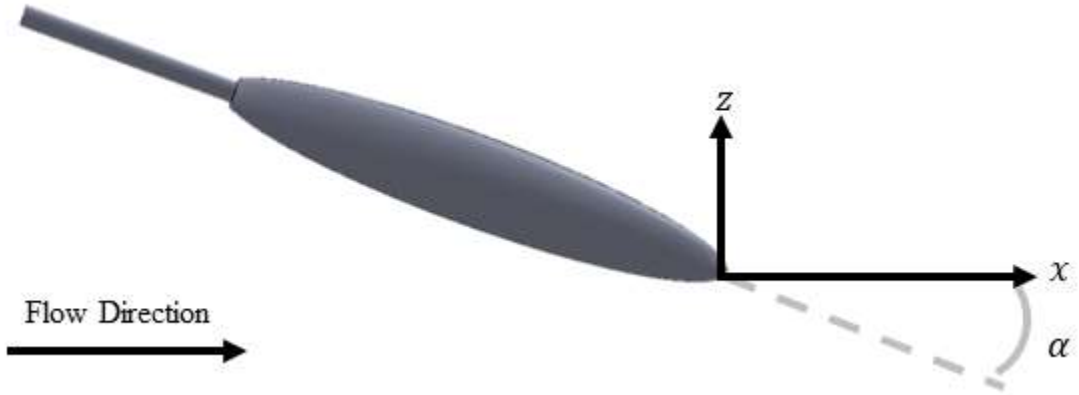

Figure 4: The coordinate system used in the present experiment with the origin at the tail of the body. Per the right-hand rule, the positive y-axis extends into the page.

Previous studies reference the forward-most point of the spheroid as $x/L = 0$ and the rear-most point as $x/L = 1.0$. However, since this is a wake study, it is more useful to reference the point on the body furthest downstream (i.e. the origin shown in Figure 4 as $x/L = 0$).

The spheroid was attached to the towing carriage using a 3.7 m (12 ft) long, 0.05 m (2 in.) diameter stainless steel sting mount, shown in Figure 5. A faring, shown in red, was added in order to reduce the interference of the abruption at the attachment point of the spheroid. The depth of the spheroid is referenced to the uppermost point of the truncated end, where the sting enters the body, and also where it connects to the sting faring. In order to capture the wake fully, the location of the spheroid with respect to the free surface was varied from 0.27 m (10.5 in) to 0.74 m (29 in) over the course of the study. The sting was mounted to the towing carriage at two points using custom stainless steel shaft collars. A V-shaped stainless steel mounting structure was used to stabilize the spheroid at the rear mounting point. The full dimensions of the experimental apparatus are shown in Figure 5.

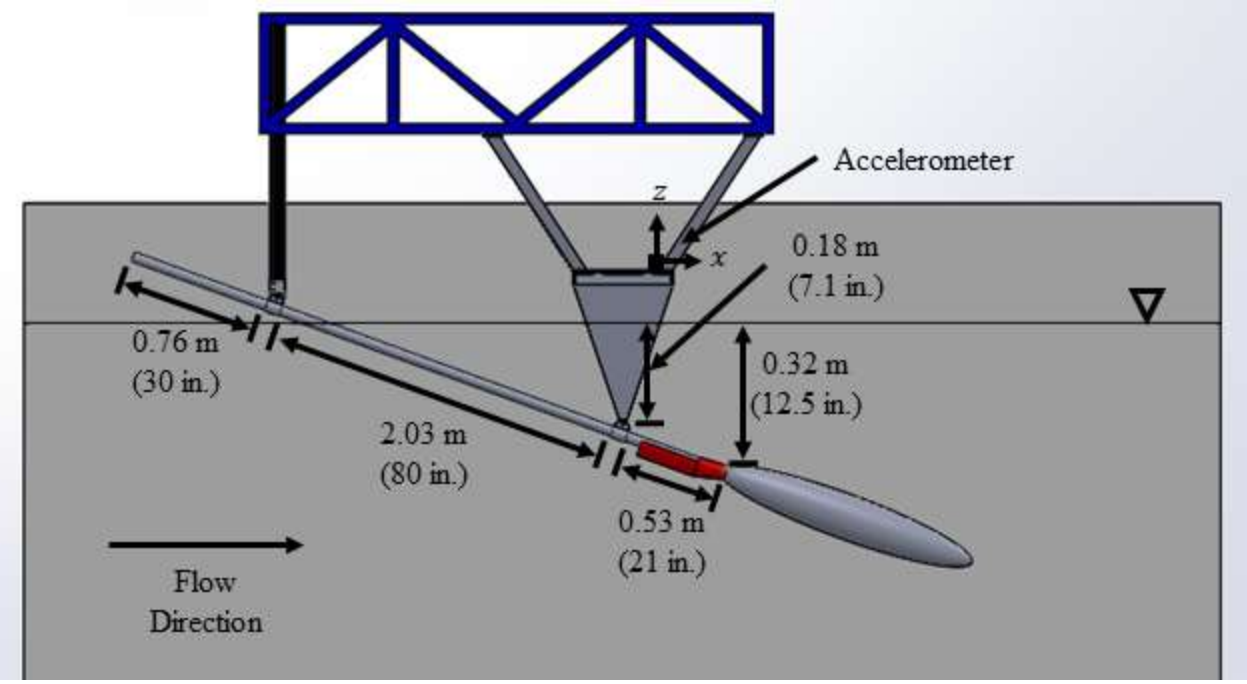

Figure 5: Dimensioned schematic of the spheroid and sting mount, attached to the towing carriage.

Instantaneous velocity measurements were made using a stationary stereo PIV system enclosed in an in-house designed and built semi-submersible housing which provided three-component velocity measurements ($V(x, y, z, t) = (u(x, y, z, t), v(x, y, z, t), w(x, y, z, t)$) for each point in the y,z measurement plane. In this presentation, only planar (2C2D) PIV results ($V(y, z, t) = v(x, y, z, t), w(x, y, z, t)$) are discussed for an inclination angle of 15° at depths of 0.32 m (12.5 in) and 0.41 m (16 in).

The system featured two 8MP PowerView™ CCD cameras. The image sensor in each camera measured 3312 px by 2488 px. The two 50 mm Nikon f/1.8G lenses were fixed inside their respective housings and aperture and focus for each were adjusted remotely. The cameras were mounted to Scheimpflug mounts and also adjusted remotely. The maximum frame rate for the cameras was 3.75 Hz which dictated the streamwise spacing between measurement planes.

The laser light sheet was formed using a Quantel EverGreen dual-pulse Nd:YAG laser capable of producing a maximum of 200 mJ per pulse at 532 nm. The beam was routed into the submersible housing using a custom light arm and the light sheet formed using a 2000 mm spherical lens and a 10 mm cylindrical lens. The light sheet thickness at center of the field of view was approximately 5 mm.

Both of the cameras and laser were housed in submersible box structures and positioned 0.99 m below the free surface. Measurements were made in the lateral (y-z) plane. The field of view was located 2.2 m from the laser. A full schematic of the measurement apparatus is shown in Figure 6.

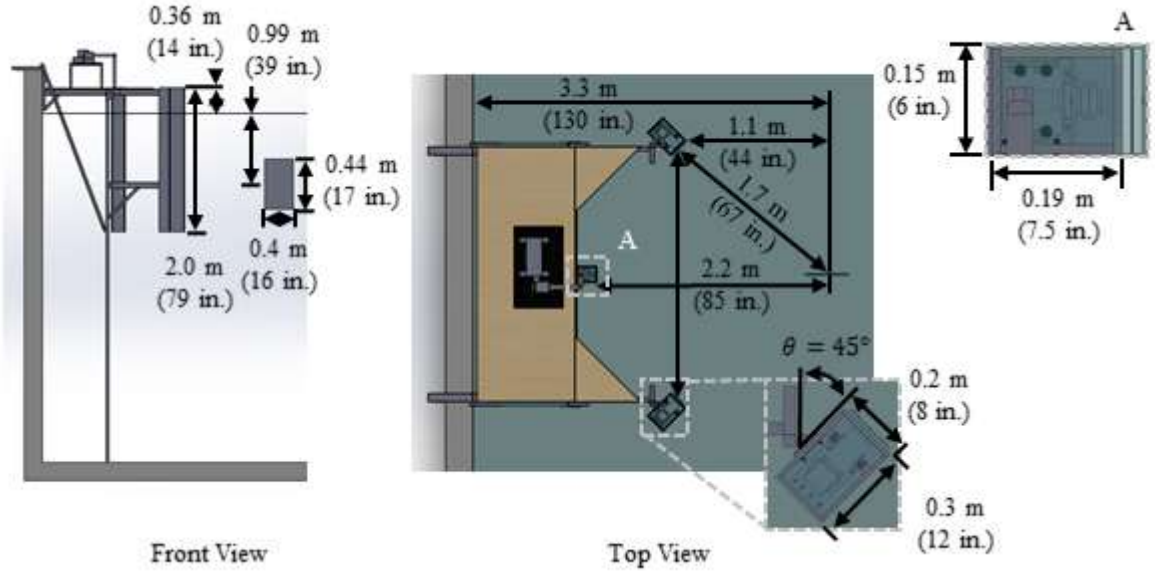

Figure 6: Dimensioned schematic of the measurement platform. The field of view is indicated by 0.51 m by 0.4 m rectangle shown to the right of the apparatus, in gray.

The entire measurement system was controlled using TSI Insight4G™. The final field of view measured 0.43 m by 0.39 m. With this field of view, using an interrogation spot size of 24 x 24 px, a vector spacing of 1.9 mm was obtained.

For each run, the carriage was accelerated from its initial position, approximately 15.2 m (50 ft.) upstream of the field of view. Once at test speed, the carriage passed an optical trigger located 9.5 m (31.3 ft.) from the field of view. This initiated image capture from the PIV system. Before each run, the flow field was seeded using Potters Industries Spherical^{TM} hollow glass microspheres, which were, for the time scale of the experiment, neutrally buoyant. For each run, or traverse of the tank by the model, the time, carriage speed, acceleration, and optical trip were coordinated in time. The optical trigger provided a definitive location in space. From the precise timing of image capture and the carriage speed, the images were correlated to a downstream distance and time. The maximum image capture rate for the system is 7.5 Hz. Since two images are required to produce a single realization, the realization frequency is 3.75 Hz, providing between 150 and 300 realizations per run, depending on the carriage speed. Five runs were conducted for each combination of test parameters.

The Reynolds numbers tested ranged from $Re_L = 5.0 \times 10^5$ to 4.2×10^6 at angles of attack of 15° and 20°. These Reynolds numbers correspond to a carriage speed, U_c, of 0.36 m/s and 3.06 m/s respectively. Table 1 provides a sample of the different test parameters used in each run.

Table 1: Example testing parameters for data collection at varying parameters

	Re_L	U_c (m/s)	U_c (ft/s)	# of Images
$\alpha = 15°$	5.00E+05	0.36	1.20	299
	1.00E+06	0.73	2.39	249
	4.20E+06	3.06	10.05	149
$\alpha = 20°$	5.00E+05	0.36	1.20	299
	1.00E+06	0.73	2.39	249
	4.20E+06	3.06	10.05	149

Only the results from the case at 15° and $Re_L = 5.0 \times 10^5$ are presented in this study.

The processing scheme used in Insight4G™ used a final interrogation spot size of 24 px by 24 px, corresponding to an area of approximately 3.7 mm by 3.7 mm in the flow field. A 50% overlap between interrogation windows was used. The images were preprocessed with a local mean filter and Gaussian filter. The postprocessor used local vector validation and filled holes in the flow field with a recursive local mean filling method. A detailed description of the processing scheme can be found in Appendix A.

Results and Discussion

Wake Characterization

In this section, the case of $Re_L = 0.5 \times 10^6$ at a 15° angle of inclination is discussed. Figure 7 shows a profile view of the spheroid in the x-z plane. The flow is travelling from left to right. The wake trail, representing the approximate center of the wake behind the spheroid, is shown as a dashed line that follows downstream of the body of the spheroid. As x/L increases, the wake moves downward in the -z direction.

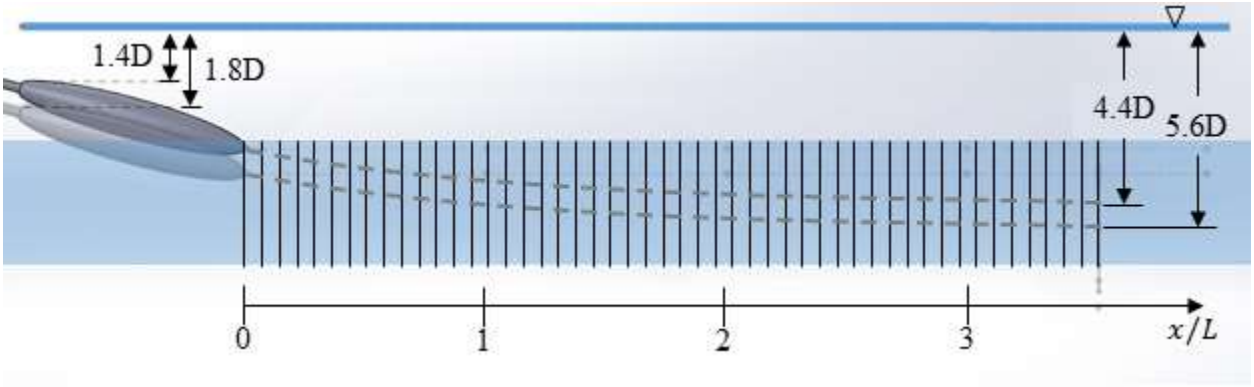

Figure 7: Wake progression behind a prolate spheroid indicated by grey dashed line. Measurement depth indicated with respect to the free surface at 1.4D (0.32 m) and 1.8D (0.41 m). The numerous black vertical lines indicate the height of the field of view and the streamwise spacing, approximately 0.1 m (3.8 in.) at the speed corresponding to $Re_L = 0.5\times10^6$.

The depth of the spheroid is referenced from the upper extent of the upstream end of the body to the undisturbed free surface, as previously described and shown in Figure 5. The depth of the field of view was held constant, therefore moving the spheroid placed different parts of the wake in view at different downstream distances. The shallower of the two depths is shown at 1.4D (12.5 in.) from the free surface. This shallower depth is further from the field of view and was useful for keeping the wake in the field of view at larger downstream distances. A slightly deeper spheroid depth at 1.8D (16 in) was also tested, moving the body closer to the field of view. The deeper depth places more of the near wake in the immediate field of view. Data from both depths are discussed.

An example of the wake progression at depth of 1.4D from the free surface is shown in Figure 8. Each image shown is separated by 4.27 s starting at $x/L = 0$ up to $x/L = 5.6$. The conversion from t to x/L is shown in Equation 2.

$$x/L = \frac{nU_c}{fL} = \frac{tU_c}{L} \tag{2}$$

Where n is the number of realizations (i.e. moment in space and time) since spheroid passage, f is the camera capture frequency in Hz, and t is the time since spheroid passage. As the spheroid passes, the wake begins to appear at the top of the field of view, indicated by the appearance of the downward jet of flow, shown in blue. The bulk of the wake proceeds to move into the field of view until the majority of the wake is visible at $t_0 + 8.5$ s ($x/L = 2.3$). The positive upward velocity created by the vortices is shown in yellow-orange. The wake continues its bulk movement towards

the bottom of the field of view and reduces in strength until $t_0 + 21.3$ s (x/L = 5.6) where the wake becomes largely incoherent and settles towards the bottom of the field of view. A similar path is observed at a spheroid depth of 1.8D, however, the wake appears in the field of view approximately two image frames earlier and begins to move out of the vertical extent of the field of view at an earlier realization.

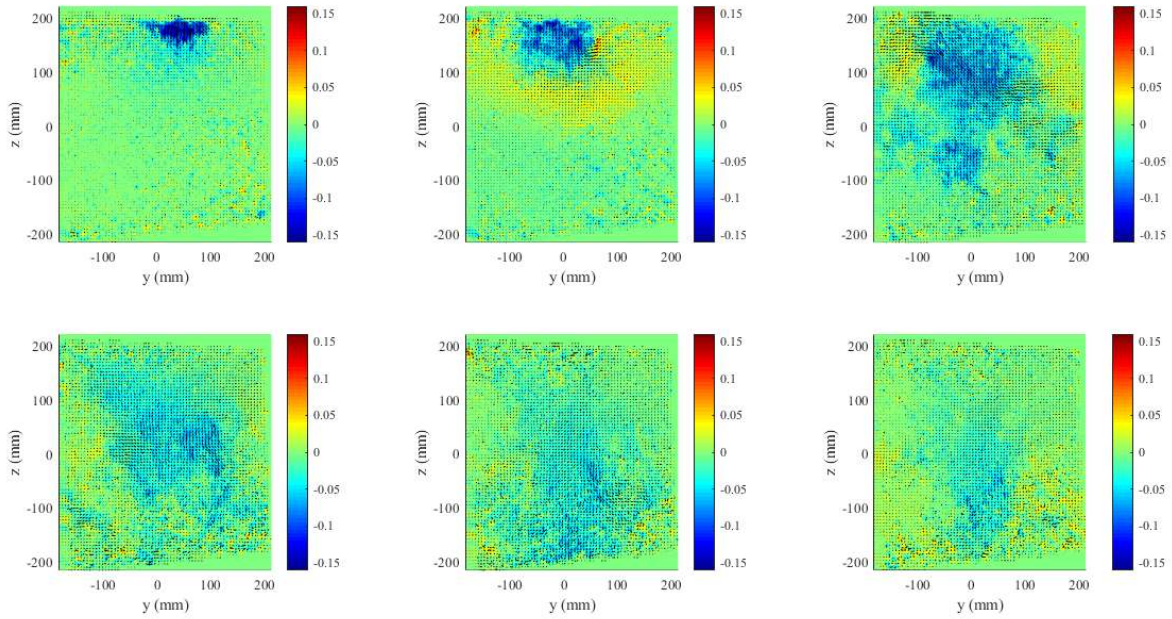

Figure 8: A contour plot of the vertical component of velocity, w showing the prolate spheroid wake progression from x/L = 0 to x/L = 5.6 (21.3 s elapsed) for $Re_L = 0.5 \times 10^6$ and $\alpha = 15°$. Spheroid depth located at 1.4D.

The accepted method for determining the spatial extent of the wake is to identify the point in space for a given moment in time at which the streamwise velocity recovers to 99% of the mean flow speed [9]. However, since the streamwise velocity component was not measured, a different method was adopted. The wake was taken to be a region of the flow in which the magnitude of velocity, defined as follows:

$$V = \sqrt{v^2 + w^2} \tag{3}$$

was high, compared to the region outside the wake. In Equation 3, v is the horizontal velocity component and w is the vertical velocity component. Because of the significant variation in single realizations captured in a defined space at a single moment in time (i.e. time histories) a high-pass filter was used to identify the wake and distinguish it from the mean flow. The threshold value for the filter was set to between 1 and 1.5 standard deviations of the magnitude of the velocity, calculated from all values over an entire run. Put another way, any fluid with a magnitude of velocity less than 1-1.5 times the standard deviation of V was filtered out. Since earlier images have a low signal to noise ratio, a higher threshold for the high pass filter was necessary. The converse is true for later images. It is conceded that there is a level of subjectivity to this approach but given the significant variability indicated between realizations in a turbulent flow field and the excellent qualitative agreement with the corresponding velocity fields, it appears to describe the wake boundary quite well.

Each realization in a run was converted into a binary image. This image was then filtered using the high pass filter to extract the wake. On this filtered image, the convex hull points were determined. The convex hull is defined as the smallest convex polygon that encloses a set of points. The wake boundary was determined to be the convex hull, bounded by the convex hull points. An example of this analysis is shown graphically in Figure 9.

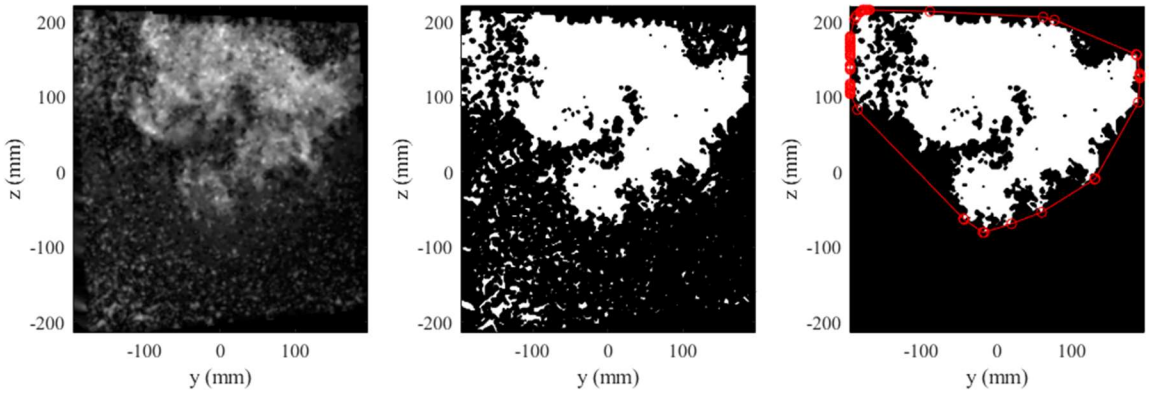

Figure 9: Image capture from wake at depth 1.8D. First image shows raw contour plot of the magnitude of velocity in grayscale. Second image shows unfiltered binary image. Third image shows high pass filtered image with convex hull. Wake represented as the convex hull or bounded region.

This convex hull analysis was performed for each realization in each run to characterize the wake movement. As x/L increases, the wake progresses from the top of the field of view to the bottom. The earlier wake boundaries show greater separation from one another and proceed to become closer together further downstream, evident by the increase in density of the wake boundary in the lower portion of the plots in Figure 10, which show the movement of the wake in the field of view for four different runs at a depth of 1.8D. A similar pattern is repeated in all runs conducted at $Re_L = 0.5 \times 10^6$. Though there is variability from realization to realization, the wake behaves in a fairly predictable manner when viewed globally.

It is evident from this from Figure 10 that the entirety of the wake is not captured in the field of view. Due to constraints in the testing facility, the time to make the significant adjustments required to adjust the field of view during data collection was not possible. However, this information will be used in follow-on experimental endeavors of the same scale. In future testing, it is recommended that the field of view be at least 1.0 m by 1.0 m in order to capture the wake fully.

The movement of the wake can be further examined by observing the vertical position of the wake over time. It is predicted from numerical studies that as the wake travels further downstream, its descent from the free surface will slow [10]. This can be observed experimentally in Figure 11. By fitting a power law curve to the vertical position of the wake over time (indicated by the solid black line), it can be determined that as the wake proceeds downstream of the spheroid, the descent of the wake begins to slow up to $t_0 = 17$ s ($x/L = 4.5$) at which point the wake begins to move beyond the field of view for this depth. The power curve fit to this data is shown as Equation 4.

$$z(t) = -2552t^{0.08168} + 2773 \tag{4}$$

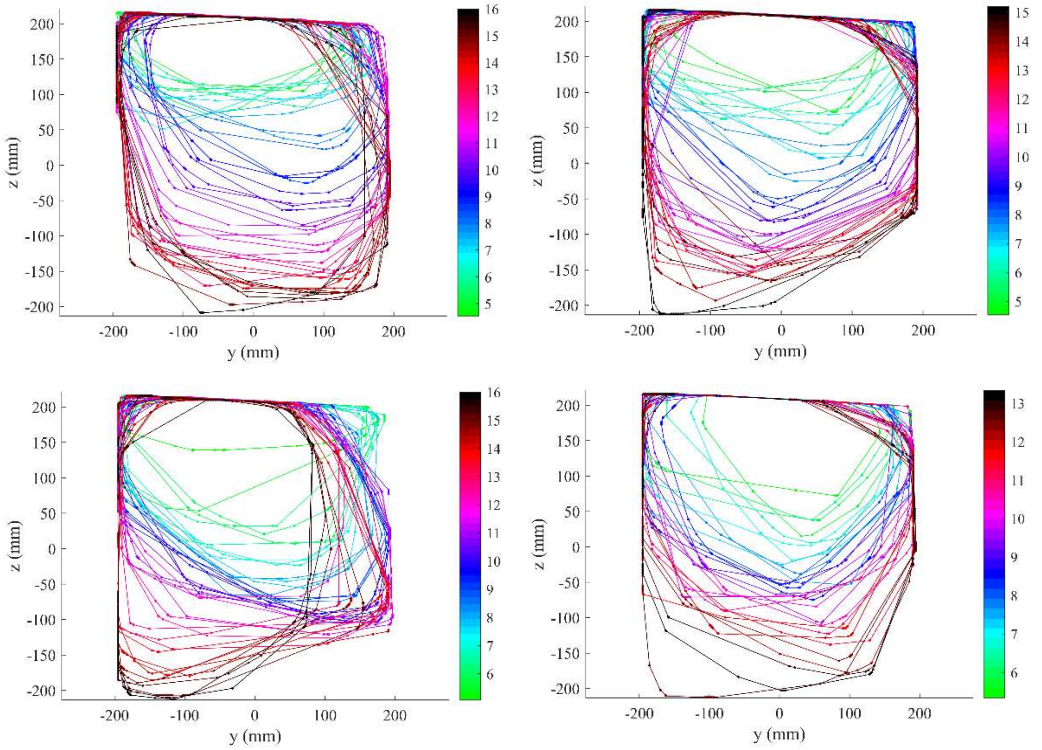

Figure 10: Wake boundary progression over time for four different runs, each at 15° angle of inclination and $Re_L = 0.5 \times 10^6$. The color gradient indicates the elapsed time from t_0.

It is important to note that the value of z in Figure 11 and Equation 4 are relative to the vertical distance from the tail of the spheroid, which is the downstream-most point on the spheroid. Therefore, $z = 0$ mm is the vertical position of the tail of the spheroid, as shown in Figure 4. Using Equations 2 and 4 for a given downstream distance, the minimum depth of field of view to capture the wake at a desired elapsed time can be obtained.

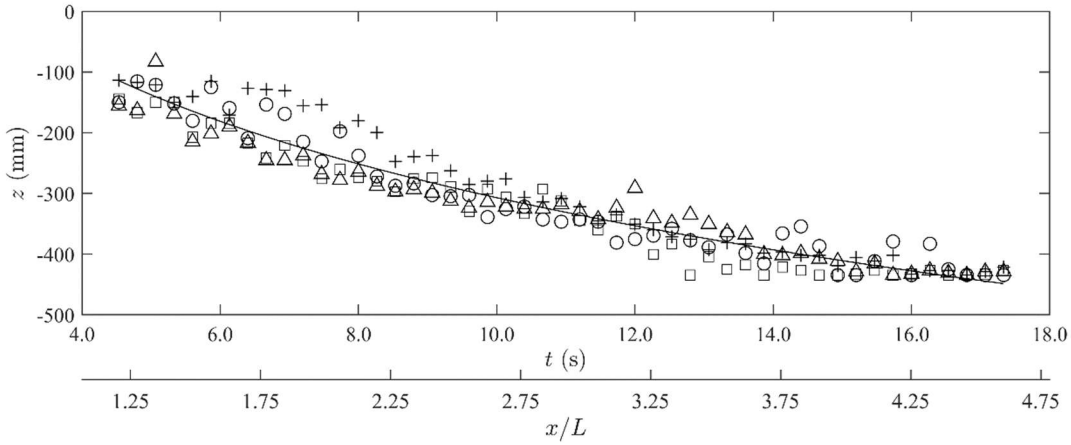

Figure 11: Vertical position of the wake in the field of view as a function of time and downstream distance for data collected at 1.8D from the free surface at $Re_\ell = 5.0 \times 10^5$ and $\alpha = 15°$. The marker symbols indicate data from different runs. The solid line is a power-law curve fit applied to the data.

Since the wake moves out of the field of view, it is difficult to determine the positional stability. However, from the data collected, the wake does follow a general pattern up to approximately $t_0 +$ 17 s (x/L = 5) at which point the wake begins to move out of the vertical extent of the field of view. This pattern is evident in both Figure 10 and 11. Though variability is evident, the wake still follows a predictable pattern when considered from the perspective of the larger measurement region.

Vortex Characterization

According to Bhagwat and Ramasamy, measurement in the region of the core of a vortex is inherently difficult due to a seed particle void created by the strong swirling motion and variations in local velocity due to turbulence [11]. Thus, using the methodology they developed for helicopter rotor wake research, a vortex model was fit to the experimental observations in order to more accurately estimate the vortex properties. Three vortex models were fit to the experimental data, as described by Leishman [12]. The first was the Lamb-Oseen model generally used for laminar vortices:

$$u_\theta = \frac{\Gamma}{2\pi r}\left(1 - e^{-a\left(\frac{r}{R}\right)^2}\right) \tag{4}$$

Here u_θ is the tangential velocity, sometimes called the *swirl velocity*, Γ is the circulation, r is the radial coordinate, a is a coefficient equal to 1.25643, and R is the radius of the vortex. The second vortex model used was the Scully Vortex model generally representative of turbulent vortices:

$$u_\theta = \frac{\Gamma}{2\pi \frac{r}{R}}\left(\frac{\frac{r}{R}}{1 + \left(\frac{r}{R}\right)^2}\right) \tag{5}$$

The third model used was developed by Vatistas et al. generally describing vortices in the transition region:

$$u_\theta = \frac{\Gamma}{2\pi R}\left(\frac{\frac{r}{R}}{\sqrt{1 + \left(\frac{r}{R}\right)^4}}\right) \tag{6}$$

All models were applied to each vortex using a non-linear least-squares fit algorithm as described by Zhou et al. [13]. The specific procedure used in the present study is as follows.

First, for each realization the v, w velocity field was plotted showing streamlines and velocity vectors. Additionally, the local λ_{ci} maxima, an established means of vortex identification, were plotted in order to better identify the vortex region. The λ_{ci} values were calculated using the methodology described by Zhou et al. [14]. A representative case is shown in Figure 12.

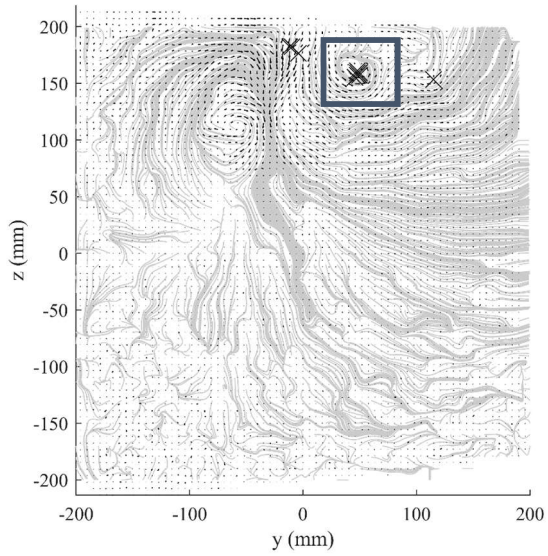

Figure 12: An example of the velocity field representation, including streamlines and velocity vectors, used to identify the vortex of interest. The black "x" marks indicate locations of maximum λ_{ci} value, which indicate the presence of a vortex. The box indicates the user-defined subregion shown in the next figure. Note: No λ_{ci} maxima are shown in the vicinity of the strong vortex on the left hand-side of the wake because it has an opposite sign (i.e. it is rotating in the opposite direction) from the one shown on the left.

From this figure, a subregion is identified surrounding the vortex of interest. A sensitivity analysis was conducted to determine the extent to which the subregion selected influenced the model fit result. It was determined that the selection of a particular subregion influenced the residual norm for the fit to a small degree but had negligible influence on the values of the resulting vortex parameters.

Once the subregion was identified, the initial guess values were solicited or calculated directly from the experimental data. The vortex model fit algorithm, developed by Lust et al. requires guess values for the centroid position (y_c, z_c), the circulation, Γ the vortex radius, r and the convective velocity, v_c, w_c [15]. The centroid position was identified by visual inspection as shown in Figure 13, which the minimum velocity magnitude marked on the figure with a red "x" to assist the user in identifying a region close to the vortex center.

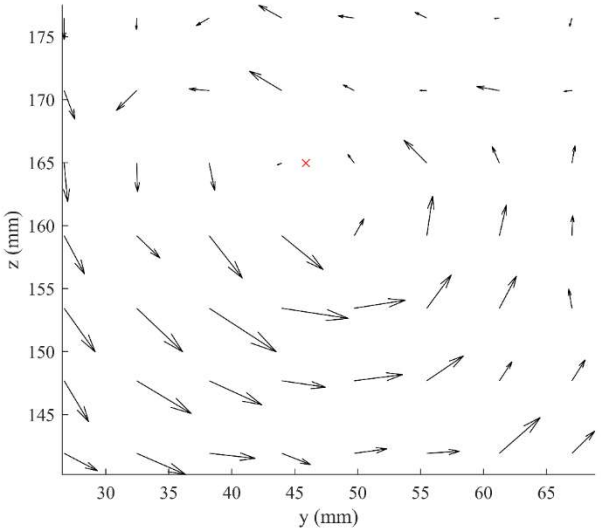

Figure 13: An example of the subregion extracted from the previous figure, corresponding to the area enclosed the box. The red "x" mark indicates the position of the minimum velocity magnitude and is intended to guide the user in identifying the guess value for the vortex centroid position.

From the guess centroid location, the velocity profile of the vortex was extracted and plotted, as shown in Figure 14.

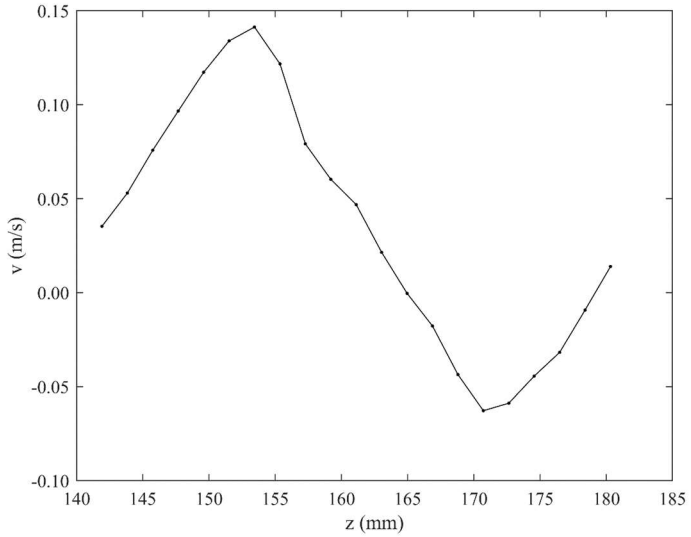

Figure 14: An example of the velocity profile extracted from a vertical line, coincident with the vortex centroid guess value identified in the previous step of the algorithm, bisecting the vortex. The guess value for the radius is calculated by taking the straight-line distance between the point of maximum and minimum velocity (i.e. the vortex diameter) and dividing by two.

The points of maximum and minimum velocity were identified to estimate the vortex radius (i.e. half the straight-line distance between these two points). From this radius, the guess value for the circulation was calculated using the following expression:

$$\Gamma = \iint \omega \, dA = A \sum \omega_i \tag{7}$$

Where ω_i is the vorticity at each array location within the area enclosed by the guess radius and A is the area of the circle corresponding to the guess radius. The vorticity, ω_i is calculated as follows:

$$\omega_i = \nabla \times V = \frac{\partial w_i}{\partial y_i} - \frac{\partial v_i}{\partial z_i} \tag{8}$$

Where ∇ is the gradient operator and the subscript i indicates *for each array point*. The y and z components of the vortex convection velocity were calculated from spatial averages of the subregion in each respective direction.

From the guess values, a least-squares-fit routine was used to fit each of the three vortex models to the experimental data. The fit parameters for a particular vortex were taken from the output of the model with the smallest residual norm. A sensitivity analysis was also conducted to determine the influence of result to the initial guess values, including the centroid selected by the user. Within the range of perturbation ($\pm 10\%$ for centroid values, $\pm 50\%$ for circulation and radius values, and $\pm 100\%$ for convection velocity values) the results varied by less than 1% in almost every case, indicating that the fit model algorithm is very robust.

Using the best of the three vortex models for each case, the location, size, strength, and time scale of the coherent vortical structures shed into the wake of the prolate spheroid at $Re_L = 0.5 \times 10^6$ at $\alpha = 15°$ was determined.

The vortex center location for several data sets at spheroid depth 1.8D is shown in Figure 15. There are two primary vortices, referred to as the left-hand side (LHS) and right-hand side (RHS) vortices. From the figure, the progression of the vortices can be followed. Though there is variation in the movement of the vortices from data set to data set, both the LHS and RHS vortices follow a predictable path that can be captured in an appropriately sized field of view. The LHS vortex appears more predictable and less variable than the RHS vortex.

In many cases, a vortex would disappear from the image and reappear in a later image resulting in some additional variability in vortex characteristics. Vortex position, while there was some local variability in centroid location, largely remained within the field of view until the vortices became unrecognizable, likely by instability and subsequent breakup.

Previous numerical investigations predicted interaction between the primary vortices in the far-wake [16]. At least within $2L$ downstream, this was not observed. It is likely that in the near wake, the downward jet maintains separation between vortices. It appears that as the wake expands and moves downstream, the vortices move away from each other and do not interact. Since the movement of the primary vortices is captured completely in the field of view before they dissipate, so it is assumed that there is no vortex interaction at $Re_L = 0.5 \times 10^6$ and $\alpha = 15°$.

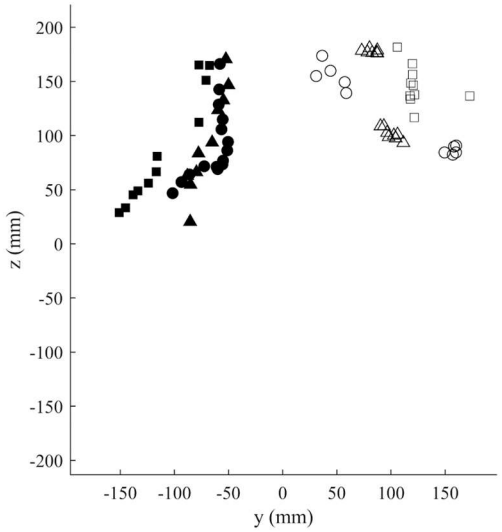

Figure 15: Vortex center location for both LHS (closed symbols) and RHS (open symbols) vortices for several runs.

According to Goody et al., the non-dimensional vortex radius at x/L = 0.776 (referenced from the forward-most point on the spheroid) will be on the order of r/D = 0.04 - 0.13 at $Re_L = 4.2 \times 10^6$ and $\alpha = 10°, 20°$ [7]. Despite a slightly different angle of inclination and a difference in Reynolds number of approximately an order of magnitude, the results of the present study compare very favorably with these.

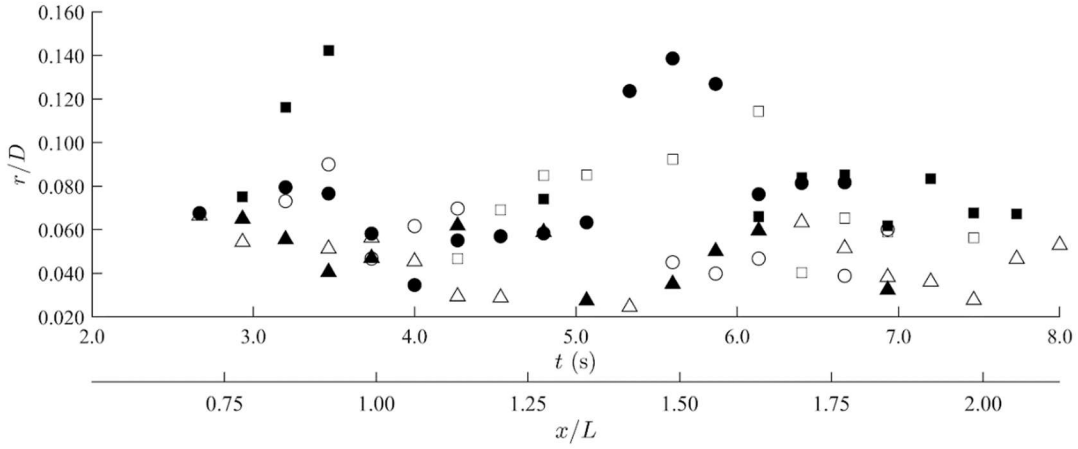

Figure 16: Vortex radius normalized by spheroid diameter plotted as a function of time and downstream distance for several data sets. Black markers represent the LHS vortex and white markers represent the RHS vortex. Different symbols represent different runs, albeit with the same experimental parameters.

As previously discussed, as x/L increases the wake expands. It expected that as the wake expands, the size of the vortices will also expand. However, this is not observed in Figure 16. The figure shows a relatively constant vortex radius at approximately r/D = 0.065.

The strength of the vortices is determined by the magnitude of the circulation non-dimensionalized by the spheroid length and towing speed, $|\Gamma|/U_{tow}L$. Figure 17 shows $|\Gamma|/U_{tow}L$ for several runs. It is expected that over time, the strength of the vortices will decrease due to viscous interactions and instability. Both vortices show a decrease in strength up to x/L = 1.8 at which point the circulation approaches zero. Therefore it can be assumed around x/L = 1.8, the primary vortices have dissipated and the wake is largely incoherent after this downstream distance.

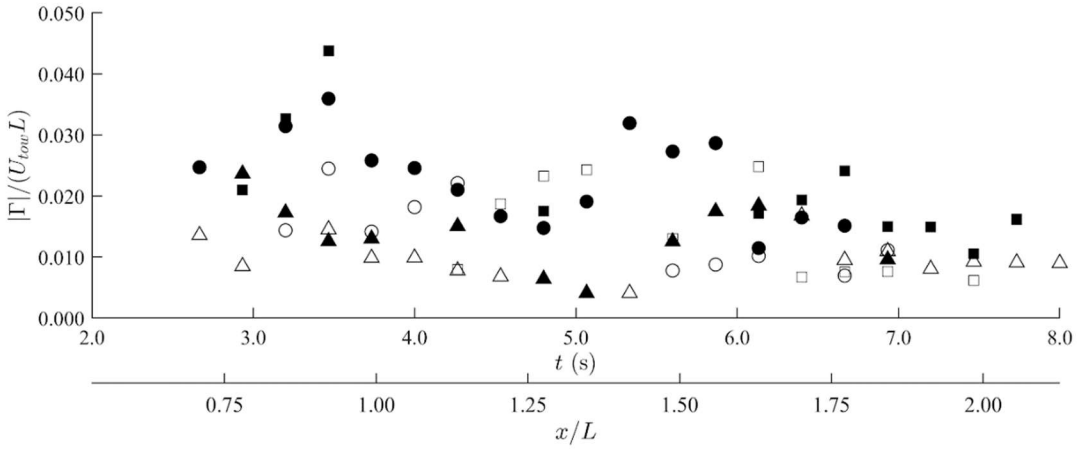

Figure 17: Magnitude of vortex circulation normalized by U_{tow} and spheroid length plotted as a function of time and downstream distance for several data sets.

As mentioned previously, the asymmetry in the flow is likely due to the asymmetric mounting of the spheroid relative to the direction of flow. It appears that the LHS vortex is generally stronger than the RHS vortex. The LHS vortex also appears more predictable and less variable than the RHS vortex, apparent in Figure 15. Despite considerable effort, this asymmetry suggests that the spheroid is perhaps asymmetric or was, more likely, asymmetrically mounted to the towing carriage. Since the LHS vortex is stronger, it is likely that the spheroid is pointing slightly into the positive y-direction.

Conclusions and Summary

Far-wake characterization of a 6:1 prolate spheroid was conducted using Particle Image Velocimetry at $Re_L = 0.5 - 4.2 \times 10^6$ and angles of incidence of 15° and 20°. The objective of this study was to obtain a fundamental understanding of the wake characteristics on this axisymmetric body at an angle of incidence in order to provide data to be used in future experimental and numerical studies. Velocity field measurements were used to determine wake position, wake stability, vortex location, size, strength, and the time scale.

Wake position was identified using the magnitude of the velocity and was shown to descend with time and downstream distance, as expected. Despite a relatively large field of view, the wake soon expanded beyond its horizontal limits. However, the vertical position of the wake was identified as a function of time up to 18 s and downstream distances of 4.75L. Despite small-scale variations in position, over the entire field of view, the vertical position was shown to be reasonably consistent with time and downstream distance – a positive result for future studies. A power-law expression was developed that can be used to predict the wake position at any time (and therefore location) downstream of the spheroid for use in future studies. Also, although it can't be stated definitively, the features in the wake, to include the downward jet and the primary vortices, also appear to be fairly positionally stable, on the scale of the field of view, giving a qualitative measure of wake location in the horizontal location. It is recommended for follow-on studies that the field of view be increased to approximately 1 m by 1 m in order to capture the horizontal and vertical extent of the wake.

The wake featured two strong, counter-rotating primary vortices in agreement with previous studies. The spatial position of the vortices were observed to follow a similar movement as the bulk of the wake. Despite local variability, the vortices followed a relatively predictable path and the vortex centroids remained in the field of view until the vortices disappeared likely due to instability and breakup. Vortex interaction, predicted in previous numerical studies, was not observed.

Vortex characteristics were estimated by fitting one of three vortex models to the experimental data using a non-linear least-squares fit algorithm. The average vortex radius was approximately r/D = 0.065 and remained relatively constant to a downstream distance of 2L, after which the primary vortices were not possible to identify. The observed size of the vortices in the present study are in agreement with previous experimental studies, which suggests that the size of the vortices may be insensitive to angle of inclination and Reynolds number.

The vortex strength was characterized by the magnitude of the circulation normalized by carriage speed and spheroid length, $|\Gamma|/U_{tow}L$. The maximum circulation was observed right after spheroid passage and as x/L increased, the circulation decreased due to viscous effects up to approximately x/L = 1.8, at which point the primary vortices became impossible to identify, perhaps due to instability and subsequent breakup. The left-side primary vortex appears more coherent and predictable than the right-side primary vortex. Despite all reasonable efforts to align the spheroid,

this is likely due to a very slight misalignment of the mount relative to the flow direction. Because the left-side primary vortex is slightly stronger, it is likely that the spheroid is slightly canted in the positive y-direction.

Future Work

A follow-on experiment will be conducted by MIDN Zachary Nygaard during academic year 2021. A towed PIV system is currently being designed and built, and will be mounted to the towing carriage in order to obtain time-averaged velocity maps for fixed positions downstream of the spheroid. These time averaged ensembles will provide more precise calculation of wake and vortex parameters as well as the calculation of turbulent statistics, which will better describe wake evolution and dissipation.

Bibliography

[1] T. C. Fu, A. Shekarriz, J. Katz and T. T. Huang, "The flow structure in the lee of an inclined 6:1 prolate spheroid," *Journal of Fluid Mechanics 269,* pp. 79-106, 1994.

[2] C. Shih, "Turbulent Wake Flow Behind a Circular Cylinder," 28 August 2002. [Online]. Available: http://www.eng.fsu.edu/~shih/succeed/cylinder/cylinder.htm. [Accessed 25 October 2019].

[3] K. Kiger, "PIV Basics: Correlation," July 2015. [Online]. Available: http://www.civil.ist.utl.pt/~ruif/SUMMER_SCHOOL/presentations/PIV_basics_correlation_final.pdf. [Accessed 06 May 2020].

[4] H. U. Meier and H. P. Kreplin, "Experimental Investigation of the Transition and Separation Phenomena on a Body of Revolution," in *International Symposium on Turbulent Shear Flow*, London, 1979.

[5] K. M. Barber and R. Simpson, "Mean Velocity and Turbulence Measurements of Flow Around a 6:1 Prolate Spheroid," *Office of Naval Research Applied Hydrodynamics Research Program,* 1990.

[6] S. Ahn and R. Simpson, "Cross-flow separation on a prolate spheroid at angles of attack," *In 30th Aerospace Sciences Meeting and Exhibit,* p. 428, 1992.

[7] M. Goody, R. Simpson and M. Engel, "Mean velocity and pressure and velocity spectral measurements within a separated flow around a prolate spheroid at incidence," *In 36th AIAA Aerospace Sciences Meeting and Exhibit,* p. 630, 1998.

[8] C. J. Chesnakas and R. L. Simpson, "Detailed investigation of the three-dimensional separation about a 6-1 prolate spheroid," *AIAA Journal 35,* pp. 990-999, 1997.

[9] S. B. Pope, Turbulent Flows, Cambridge University Press, 2001.

[10] M. Jemison, "6:1 Prolate Spheroid: Wake Simulations," *Unpublished Document,* 2019.

[11] M. J. Bhagwat and M. Ramasamy, "Effect of Tip Vortex Aperiodicity on Measurement Uncertainty," *Experiments in Fluids,* vol. 53, no. 5, pp. 1191-1202, 2012.

[12] G. J. Leishman, Principles of Helocopter Aerodynamics, New York: Cambridge University Press, 2006, pp. 586-588.

[13] M. Ramasamy, R. Paetzel and M. J. Bhagwat, "Aperiodicity Correction for Rotor Tip Measurements," Army Research Development and Engineering Command, Aviation Aeroflight Dynamics Directorate, Moffett Field, 2011.

[14] J. Zhou, R. J. Adrian, S. Balachandar and T. M. Kendall, "Mechanisms for Generating Coherent Packets of Hairpin Vortices in Channel Flow," *Journal of Fluid Mechanics,* vol. 387, pp. 353-396, 1999.

[15] E. E. Lust, K. A. Flack and L. Luznik, "Survey of the near wake of an axial-flow hydrokinetic turbine in quiescent conditions," *Renewable Energy,* vol. 129, pp. 92-101, 2018.

[16] H. I. Andersson, F. Jiang and V. L. Okulov, "Instabilities in the wake of inclined prolate," *Computational Methods in Applied Sciences Computational Modelling of Bifurcations and Instabilities in Fluid Dynamics,* pp. 311-352, 2018.

[17] J. W. R. J. Adrian, Particle Image Velocimetry, Cambridge: Cambridge University Press, 2011.

[18] A. J. S. A. Ashok, "The Turbulent Wake of a Submarine Model in Pitch and Yaw," *30th Aerospace Sciences Meeting and Exhibit,* p. 428, 1992.

[19] L. Bertuccioli, G. I. Roth, J. Katz and T. R. Osborn, "A Submersible Particle Image Velocimetry System for Turbulence Measurements in the Bottom Boundary Layer," *Journal of Atmospheric and Oceanic Technology,* vol. 16, pp. 1635-1646, 1999.

[20] R. Chevray, "The Turbulent Wake of a Body of Revolution," *Jounral of Basic Engineering,* vol. 90, pp. 275-284, 1968.

[21] C. E. Costis and D. P. Telionis, "Laser-Doppler Velocimetry and Flow Visualization of 3-D Flows," *IUTAM Symposium,* 1984.

[22] C. E. Costis, D. P. Telionis and N. T. Hoang, "Laminar separating flow over a prolate spheroid," *Journal of Aircraft,* vol. 29, no. 9, pp. 810-816, 1989.

[23] M. C. Goody, R. L. Simpson and C. J. Chesnakas, "Separated Flow Surface Pressure Fluctuations and Pressure-Velocity Correlations on Prolate Spheroid," *AIAA Journal,* vol. 38, no. 2, pp. 266-274, 2000.

[24] G. K. El Khoury, H. I. Andersson and B. Pettersen, "Wakes behind a prolate spheroid in crossflow," *Journal of Fluid Mechanics,* vol. 701, pp. 98-136, 2012.

[25] T. Han and V. C. Patel, "Flow separation on a spheroid at incidence," *Journal of Fluid Mechanics,* vol. 92, no. 4, pp. 643-657, 1979.

[26] F. Jiang, J. P. Gallardo, H. I. Andersson and Z. Zhang, "The transitional wake behind and inclined prolate spheroid," *Physics of Fluids,* vol. 27, no. 9, p. 093602, 2015.

[27] F. Jiang, H. I. Andersson, J. P. Gallardo and V. L. Okulov, "On the peculiar structure of a helical wake vortex behind an inclined prolate spheroid," *Journal of Fluid Mechanics,* vol. 801, pp. 1-12, 2016.

[28] J. J. Radice, P. J. Ellsworth, M. A. Romano, N. Lazarus and S. S. Bedair, "On the use of discontinuous nonlinear bistable dynamics to increase the responsiveness of energy harvesting devices," *Mechanics Research Communications,* vol. 84, pp. 49-54, 2017.

[29] M. Ramasamy, B. Johnson and J. G. Leishman, "Turbulent Tip Vortex Measurements Using Dual-Plane Stereoscopic Particle Image Velocimetry," *AIAA Journal,* vol. 47, no. 8, pp. 1826-1840, 2009.

[30] K. C. Wang, H. C. Zhou, C. H. Hu and S. Harrington, "Three-dimensional separated flow structure over prolate spheroids," *Proc. R. Soc. Lond. A,* vol. 429, no. 1876, pp. 73-90, 1990.

[31] T. Wetzel, R. L. Simpson and C. J. Chesnakas, "Measurement of Three-Dimesnional Crossflow Separation," *AIAA Journal,* vol. 36, no. 4, pp. 557-564, 1998.

Appendix A: Processing PIV Images according to Julio Barros, PhD
Written by Ethan Lust, PhD

Goal: Minimize the number of interpolated vectors.

Overall scheme:

1. Look at one image pair per run
2. Use the "default" Processing and Post-processing algorithms to run a first pass, not smoothing during vector conditioning.
3. If it looks like some of the good vectors are getting thrown out, adjust
    a. The *Gaussian Peak Threshold* to 1.0100
    b. Increase the *Velocity Tolerance dU* to 3 for both *Vector Local Validation* stages
4. Copy the vector statistics into the lab book spreadsheet
5. Once you are satisfied with the processing and post-processing schemes, turn on the smoothing for vector conditioning.
6. Batch process the run!

Specific steps

1. From the *Exp Tree* tab in Insight, select the image pair(s) to process.
2. Under the *Processing* tab, create at **Region of Interest**
    a. Remove the black border (of doom) by dragging a square around the processing region using the left-mouse button
3. Skip over **Pre-Processing**
4. **Preprocessing Mask** can be used to mask a feature in the image.
5. Under **Processing** select *create new* from the dropdown menu.
6. Name the processing scheme. Julio suggests using the Grid Engine, *Recursive* and the size of the Final Spot Dimensions. In this case, the name is *Recursive32by32*.
7. Set the following
    a. PIV Algorithm to *Classic PIV* (default)
    b. PIV Plugins
        i. *Grid Engine* set to *RecrusiveNyquistGrid*
        ii. *SpotMaskEngine* set to *ZeroPadMask*
        iii. *Correlation Engine* leave set to *FFTCorrelator* (default)
        iv. *Peak Engine* leave set to *GaussianPeak* (default)
    c. *Starting Spot Dimensions* leave set to *64 by 64* (default)
    d. *Final Spot Dimensions* leave set to *32 by 32* (default)
        i. You can go back later and decrease the final spot size to improve resolution, but 32 by 32 is a good start.
    e. *Maximum Displacement* increase *dx* to 0.49 (maximum)

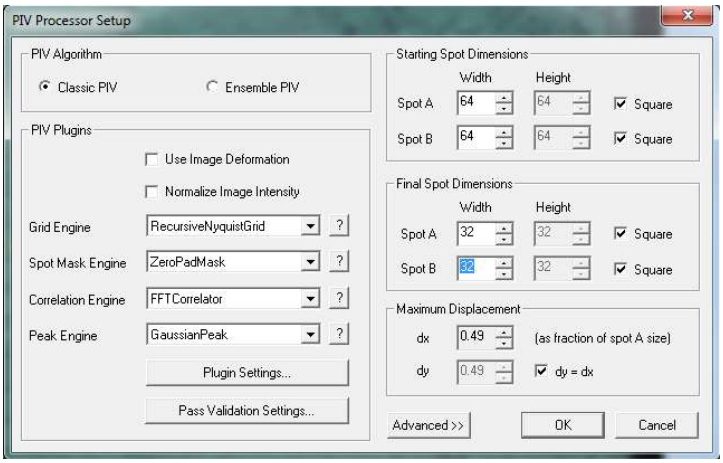

8. Under *Plugin Settings* click on *Threshold* under *Gaussian Peak* and change from the default value (1.5000 I believe) to 1.0500 to start. If, after running the processing scheme, it looks as though several good vectors are being marked as bad, lower the threshold to 1.0100 to keep more of the good vectors.

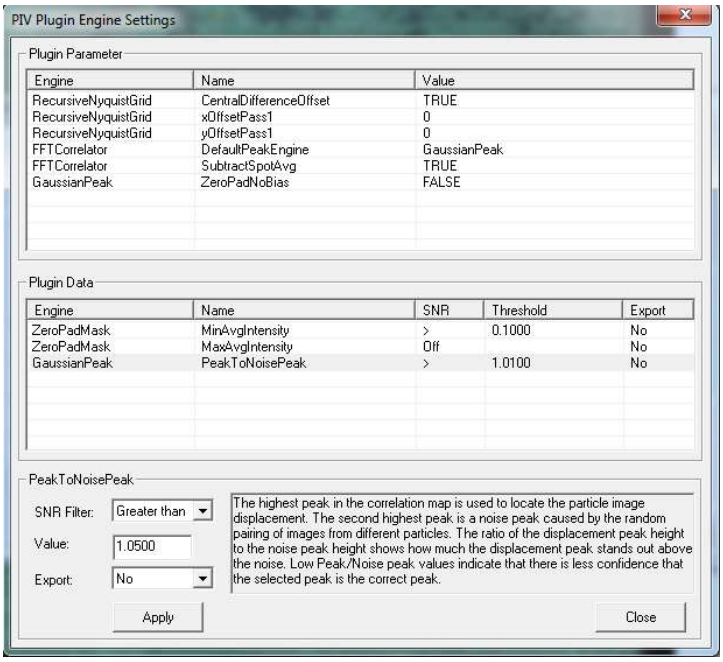

9. At this point, the processing algorithm will provide vectors. However, there is certainly more to do.
10. Under *Pass Validation Settings*
    a. Between *Input* and *Output* include two *Local Validations* followed by one *Vector Conditioning*

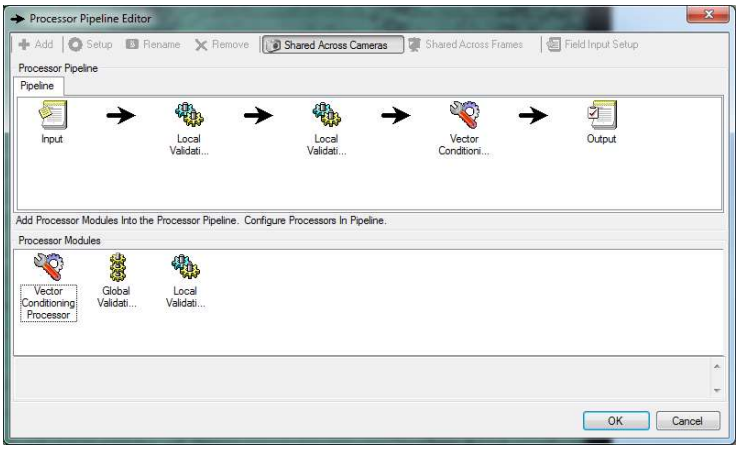

11. For the first *Local Validation* set the following:
    a. *Method* leave set to *Median Test* (default)
    b. *Neighborhood Size* set to 3x3
    c. *Bad Vector Replacement* check *By Valid Secondary Peak*

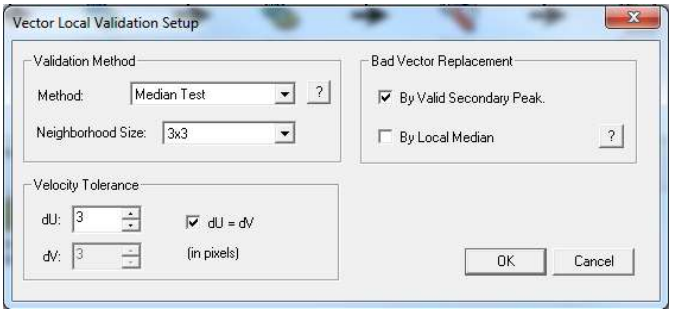

12. For the second *Local Validation* set the following:
    a. *Method* leave set to *Median Test* (default)
    b. *Neighborhood Size* set to 5x5 (default)
    c. Under *Bad Vector Replacement* check *By Valid Secondary Peak* and *By Local Median*

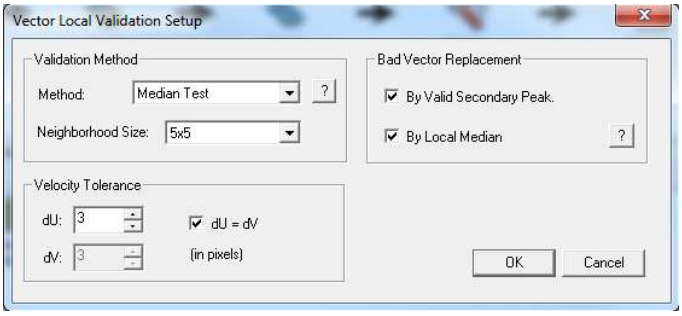

13. For the *Vector Conditioning* set the following:
    a. Under *Filling Holes* set the *Neighborhood Size* set to *3x3*
    b. For *Filling Method* set *Use Local Mean* and ensure *Recursive Filling* is checked
    c. Under *Smoothing (Low-Pass Filtering)* do the following:

i. Check the box next to *Perform Smoothing after Filling Holes*
ii. Set *Filter Size* to *3x3*
iii. Set *Sigma* to 1.1

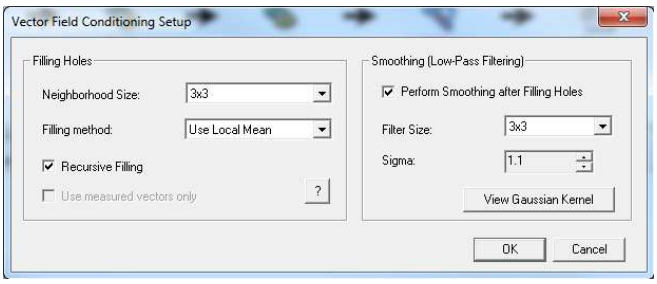

14. Under *Advanced* in the *PIV Processor Setup* window
    a. Check the box next to *Enable Rohaly-Hart Analysis* and increase the Number of Passes to 3.
    b. Increase the *Number of Secondary Peaks* under *Export Options* to 3.
15. For **Post-processing** set things up exactly the same way except:
    a. For the *Vector Conditioning* set the following
        i. For *Filling Method* set *Use Local Mean* and ensure *Recursive Filling* is checked
        ii. Under *Smoothing (Low-Pass Filtering)* do the following:
            1. For a first pass look at a data set leave this box unchecked otherwise you won't be able to tell how many vectors were interpolated (it will say 100%)
            2. For the final validation, once you've got everything set as you want it,
                a. Set *Filter Size* to *3x3*
                b. Set *Sigma* to 0.8